Magnetic exchange parameters and anisotropy of the quasi-two-dimensional antiferromagnet $NiPS_3$

D. Lançon,[1,2,*] R. A. Ewings,[3] T. Guidi,[3] F. Formisano,[4] and A. R. Wildes[1,†]

[1]*Institut Laue-Langevin, CS 20156, 38042 Grenoble Cédex 9, France*

[2]*Ecole Polytechnique Fédérale de Lausanne, SB ICMP LQM, CH-1015 Lausanne, Switzerland*

[3]*ISIS Pulsed Neutron and Muon Source, STFC Rutherford Appleton Laboratory, Harwell Campus, Didcot, OX11 0QX, United Kingdom*

[4]*Consiglio Nazionale delle Ricerche, Istituto Officina dei Materiali, Operative Group in Grenoble, F-38042, Grenoble, France*

(Received 4 August 2018; revised manuscript received 21 September 2018; published 9 October 2018)

Neutron inelastic scattering has been used to measure the magnetic excitations in powdered $NiPS_3$, a quasi-two-dimensional antiferromagnet with spin $S = 1$ on a honeycomb lattice. The spectra show clear, dispersive magnons with a ∼7 meV gap at the Brillouin zone center. The data were fitted using a Heisenberg Hamiltonian with a single-ion anisotropy assuming no magnetic exchange between the honeycomb planes. Magnetic exchange interactions up to the third intraplanar nearest neighbor were required. The fits show robustly that $NiPS_3$ has an easy-axis anisotropy with $\Delta = 0.3$ meV and that the third nearest neighbor has a strong antiferromagnetic exchange of $J_3 = -6.90$ meV. The data can be fitted reasonably well with either $J_1 < 0$ or $J_1 > 0$, however, the best quantitative agreement with high-resolution data indicates that the nearest-neighbor interaction is ferromagnetic with $J_1 = 1.9$ meV and that the second nearest-neighbor exchange is small and antiferromagnetic with $J_2 = -0.1$ meV. The dispersion has a minimum in the Brillouin zone corner that is slightly larger than that at the Brillouin zone center, indicating that the magnetic structure of $NiPS_3$ is close to being unstable.

DOI: 10.1103/PhysRevB.98.134414

I. INTRODUCTION

$NiPS_3$ belongs to a family of quasi-two-dimensional antiferromagnets [1,2]. The family have layered structures with the 2+ transition metal ions forming a honeycomb lattice in the *ab* planes. The compounds in the family are isostructural, all having the monoclinic space group $C\frac{2}{m}$ [3], and the *ab* planes are weakly bound by van der Waals forces.

The compounds show a variety of physical properties that make them interesting. Other elements and molecules can be intercalated between the planes and the compounds have been extensively studied as potential battery materials [2]. The compounds are Mott insulators, however, recent experiments show that they can become metallic under an applied pressure [4,5], offering insight into electronic band theory and potentially into high-temperature superconductivity. Individual layers can be delaminated, attracting the interest of the graphene community [6–8].

They are also good model systems for testing the theory of magnetism in low dimensions. Other members of the family include $MnPS_3$, which is a good example of a Heisenberg system [9–11], and $FePS_3$, which is a good example of an Ising system [9,12,13]. These compounds have been extensively studied for their model magnetic properties. A less-studied member of the family is $CoPS_3$, which appears to have an XY-like anisotropy [14]. $NiPS_3$ makes up the fourth member of the family. Combined, the family represent an excellent platform for the study of magnetism on a two-dimensional honeycomb lattice, with spin $S = 5/2$, 2, 3/2, and 1 for $MnPS_3$, $FePS_3$, $CoPS_3$, and $NiPS_3$, respectively.

$NiPS_3$ has the highest Néel temperature of the family with $T_N = 155$ K, forming the antiferromagnetic structure shown in Fig. 1 [15]. The magnetic structure has a propagation vector of $\mathbf{k}_M = [010]$, forming zigzag ferromagnetic chains parallel to the crystallographic **a** axis that are antiferromagnetically coupled along the **b** axis and ferromagnetically coupled along the **c** axis. The moments are collinear with their common axis being almost parallel to **a**.

The magnetic susceptibility has a very broad maximum at ∼270 K, well above the Néel temperature [9,15,17], which is a common feature of low-dimensional magnets [18]. The susceptibility only becomes Curie-Weiss-like above ∼450 K, indicating that critical fluctuations are very strong in this compound. The data suggest that $NiPS_3$ is a good example of a two-dimensional magnet.

The paramagnetic susceptibility of $NiPS_3$ has a large, negative Curie constant, Θ [9]. A correlated effective field model has been used to analyze the susceptibility to determine a nearest-neighbor antiferromagnetic exchange interaction of $J_1 = -5.0$ meV and an easy-plane single-ion anisotropy of $\Delta = -1.39$ meV [17]. There is some debate as to the nature of the anisotropy. Initial measurements showed that the paramagnetic susceptibility was anisotropic [9,17], while more recent measurements showed it to be isotropic [15]. The discrepancy was attributed to the handling of the samples, with the act of gluing a sample to a support shown to affect the magnitude of the susceptibility [15]. This dependence, potentially linked to some form of magnetostriction or deformation of the sample, suggests that $NiPS_3$ may be close to a magnetic instability.

Neutron inelastic scattering has previously been used to determine the magnetic exchange parameters of $MnPS_3$ [10]

*Current address: Laboratory for Neutron Scattering and Imaging, Paul Scherrer Institute WHGA/150, 5232 Villigen PSI, Switzerland.

†wildes@ill.fr

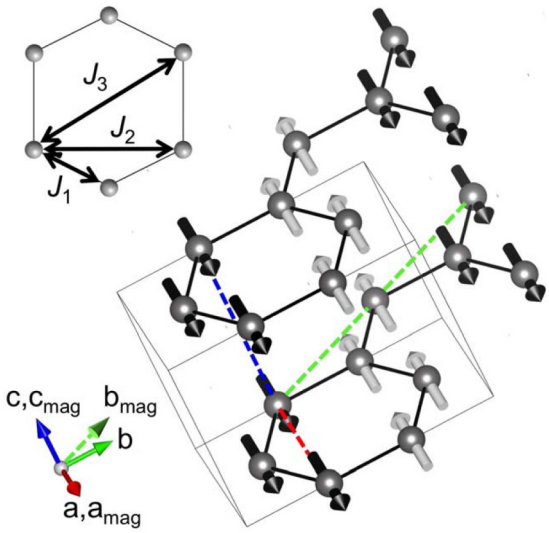

FIG. 1. The magnetic structure of $NiPS_3$ with the crystallographic unit cell, and the unit cell used in the calculation of the magnetic dynamic structure factor. The insert shows the exchange interactions between the first, second, and third nearest intraplanar neighbors. The figure was created using the VESTA program [16].

and $FePS_3$ [12,13]. The technique gives direct access to the dynamic structure factor, $S(\mathbf{Q}, E)$, hence allowing the Hamiltonian to be tested and parameterized. In this paper, we report neutron inelastic scattering experiments on powdered samples of $NiPS_3$. Estimates for the magnetic exchange parameters and anisotropy have been determined and are compared in a consistent manner with those for $MnPS_3$ and $FePS_3$. The experiments and analysis closely follow those previously reported for powdered $FePS_3$ [12].

II. EXPERIMENTS

Crystal samples of $NiPS_3$ were grown by a vapor transport method using protocols that have been previously explained in detail [15]. Approximately 10 grams of crystals were ground to a powder. The powdered sample was divided into three portions of approximately equal mass and each portion was compressed into a cylindrical pellet of 10 mm diameter. The three pellets were placed side by side in an aluminium envelope with their cylindrical axes being collinear.

Neutron inelastic scattering measurements were performed using the MARI [19] and MAPS [20] spectrometers at the ISIS facility, Rutherford Appleton Laboratories, UK, and using the BRISP spectrometer [21] at the Institut Laue Langevin, Grenoble. These are all direct geometry spectrometers, using a fixed incident neutron energy E_i and measuring the neutron time-of-flight to determine the final neutron energy.

MARI was used to give an overview of the magnetic excitations. Measurements were performed with incident energies $E_i = 15$, 30, 110, and 200 meV. MAPS has a longer sample-detector path length than MARI and therefore has better energy resolution for the same incident energy. It was used with $E_i = 200$ meV to study in detail the scattering at small momentum transfers and large energy transfers. BRISP is optimized for spectroscopic measurements at small scattering angles, and it was used to characterize a possible spin wave gap. Measurements were performed with $E_i = 20.45$ and 81.81 meV.

The sample temperature was controlled using a closed-cycle cryorefrigerator for the ISIS spectrometers, and a liquid helium cryostat for the BRISP spectrometer. The measurements were performed at the lowest possible temperature for the sample environment, which was 5 K for the cryorefrigerators and 1.5 K for the cryostat.

III. DATA MODELLING AND ANALYSIS

The MARI and MAPS data were reduced using the MANTID software suite [22]. The LAMP software package was used to reduce the BRISP data [23]. The data reduction involved normalizing to the incident flux, binning the data in rings with equivalent scattering angle, ϕ, subtracting a background estimated from a measurement of the empty cryostat, and a normalization of the detector efficiency from a measurement of a vanadium standard.

The MARI and MAPS spectrometers have a large detector coverage, measuring the scattering to large neutron momentum transfers Q. The phonon contribution was estimated through the Q dependence of scattering following a protocol described in the appendix. The estimated phonon contribution was then subtracted from the data and the results were taken to be the magnetic inelastic scattering.

The magnetic inelastic scattering data were then modeled and fitted using linear spin wave theory. The dynamic structure factor $S(\mathbf{Q}, E)$, used to fit the data, was derived from a Heisenberg Hamiltonian with a single-ion anisotropy:

$$H = -\sum_{i,j} J_{i,j}\mathbf{S}_i \cdot \mathbf{S}_j - \Delta \sum_i \left(S_i^z\right)^2, \qquad (1)$$

where Δ is the strength of the anisotropy and $J_{i,j}$ are the exchange interactions, with ferromagnetic exchange interactions being positive and antiferromagnetic exchange interactions being negative. The same Hamiltonian was successfully used to model the magnon spectra for $MnPS_3$ [10] and $FePS_3$ [12,13], and was used to estimate the magnetic exchange and anisotropy from the magnetic susceptibility of $NiPS_3$ [17].

The crystal structure of $NiPS_3$ is quoted to have some site disorder between the main $4g$ and the minority $2a$ sites for the Ni, and likewise for the main $4i$ and the minority $8j$ sites for the P [3]. However, it is likely that the minority contribution may be an artefact of the sample having stacking faults and refinements of the magnetic structure were not improved on including the site disorder [15]. Consequently, only the magnetic structure of the majority sites was considered in the analysis.

In keeping with previous calculations for $FePS_3$ [13], $S(\mathbf{Q}, E)$ was derived from Eq. (1) by decomposing the antiferromagnetic structure of $NiPS_3$ into four interlocking magnetic sublattices. The sublattice vectors were chosen to be slightly different to the lattice vectors for the crystallographic unit cell. Figure 1 shows the axes chosen for the calculation, with the subscript *mag* designating the axes for a primitive sublattice. The vectors $\mathbf{a} = \mathbf{a}_{\mathrm{mag}}$ and $\mathbf{c} = \mathbf{c}_{\mathrm{mag}}$, however the vectors $\mathbf{b}$ and $\mathbf{b}_{\mathrm{mag}}$ differ. In the magnetic coordinates, $|\mathbf{b}_{\mathrm{mag}}| = 2|\mathbf{a}|$ and $\gamma_{\mathrm{mag}} = 120^\circ$. The Miller indices for the two lattices are related

through the transformation

$$\begin{bmatrix} h \\ k \\ l \end{bmatrix} = \begin{bmatrix} 1 & 0 & 0 \\ 1 & 1 & 0 \\ 0 & 0 & 1 \end{bmatrix} \begin{bmatrix} h_{\mathrm{mag}} \\ k_{\mathrm{mag}} \\ l_{\mathrm{mag}} \end{bmatrix}. \tag{2}$$

The propagation vector for $NiPS_3$ is $\mathbf{k}_M = [010]$ while it is $\mathbf{k}_M = [01\frac{1}{2}]$ for $FePS_3$ [13]. Consequently, the transformation matrix given in Eq. (2) is slightly different between the two compounds [13]. Furthermore, while the matrix form of the Hamiltonian is identical between $NiPS_3$ and $FePS_3$, the matrix elements are slightly different. After applying the Holstein-Primakoff transformations, the Hamiltonian for $NiPS_3$ with its matrix elements is written as

$$\begin{aligned}
\mathbf{H}_M &= 2S \begin{bmatrix} A & B^* & C & D^* \\ B & A & D & C \\ C & D^* & A & B^* \\ D & C & B & A \end{bmatrix}, \\
A &= 2J_2 \cos(2\pi h_{\mathrm{mag}}) + 2J' \cos(2\pi l_{\mathrm{mag}}) \\
&\quad - \Delta - J_1 + 2J_2 + 3J_3 - 4J', \\
B &= \exp\left(\frac{2\pi i}{3}\left[2h_{\mathrm{mag}} + \frac{k_{\mathrm{mag}}}{2}\right]\right) \\
&\quad \times \left\{ \begin{matrix} J_1(1 + \exp(-2\pi i h_{\mathrm{mag}})) \\ +J'\begin{pmatrix}\exp(2\pi i l_{\mathrm{mag}}) \\ +\exp(-2\pi i[h_{\mathrm{mag}} + l_{\mathrm{mag}}])\end{pmatrix} \end{matrix} \right\}, \\
C &= 2J_2\left(\cos(\pi k_{\mathrm{mag}}) + \cos\left(2\pi\left[h_{\mathrm{mag}} + \frac{k_{\mathrm{mag}}}{2}\right]\right)\right), \\
D &= \exp\left(\frac{2\pi i}{3}\left[2h_{\mathrm{mag}} + \frac{k_{\mathrm{mag}}}{2}\right]\right) \\
&\quad \times \left\{ \begin{matrix} J_1 \exp\left(-2\pi i\left[h_{\mathrm{mag}} + \frac{k_{\mathrm{mag}}}{2}\right]\right) \\ +J_3\begin{pmatrix}2\cos(\pi k_{\mathrm{mag}}) \\ +\exp\left(-2\pi i\left[2h_{\mathrm{mag}} + \frac{k_{\mathrm{mag}}}{2}\right]\right)\end{pmatrix} \end{matrix} \right\},
\end{aligned} \tag{3}$$

where $J_{1,\ldots,3}$ are the exchange interactions between the first to third nearest neighbors in the ab planes, and J' is the exchange between neighbors along the **c** axis. As suggested from the paramagnetic susceptibility, the intraplanar exchange is expected to be weak due to the two-dimensional nature of $NiPS_3$ and J' was assumed to be zero in the analysis of the neutron scattering data.

The Hamiltonian matrix in Eq. (3) was then diagonalized to determine the eigenvectors, which were then used to calculate the magnetic dynamic structure factor, $S(\mathbf{Q}, E)$, and consequently the partial differential neutron cross-section. Explicit equations for the eigenvectors of Eq. (3) are given by Wheeler *et al.* [24].

The resulting neutron cross-sections were used to fit the data collected using the MARI and MAPS spectrometers. The procedure was identical to that used for $FePS_3$ and has been previously discussed in detail [12]. Summarizing briefly, experimental data were selected over a range of neutron scattering angles, ϕ, and energy transfers, E. Powder-averaged cross-sections were calculated with given exchange parameters and anisotropies for each data point in the selected range and convoluted with the instrument resolution, estimated using the CHOP utility program [25]. Both experimental data and calculation were then summed over the chosen ϕ range to give comparable one-dimensional functions of the intensity, $I(E)$. The data could then be fitted in a straight-forward manner, with J_1, J_2, J_3, and Δ as fit parameters. The fitting was performed using the Particle Swarm optimization algorithm [26], available in the IFIT optimizer library [27] written for MATLAB. The algorithm is particularly adept at finding global minima. Different ranges of (ϕ, E) were selected and fitted in order to test the uniqueness of the resulting best fit parameters.

IV. RESULTS

The neutron inelastic scattering from the magnetic fluctuations in $NiPS_3$ measured at 5 K is shown in Fig. 2. The figure shows data measured on MAPS and MARI for a selection of incident neutron energies, E_i. The data have had estimates for the phonon contribution subtracted, following the procedure in the appendix, and are plotted from a nonzero minimum energy transfer, E, such that the strong elastic scattering is not visible.

The data all show clear magnetic inelastic scattering which is particularly strong for $Q < 2$ Å^{-1}. The MARI data also showed some extra scattering, which is particularly visible for $E_i = 30$ meV within the range $1 \leqslant Q \leqslant 2$ Å^{-1} and $E \leqslant 8$ meV. The position and relative intensity of the extra scattering depended on the choice of the incident neutron energy, showing that it was due to the instrument configuration and not representative of the sample.

Strong dispersive intensity is seen at $Q \sim 0.6$ Å^{-1} and small energy transfers. Other, weaker, dispersive modes can be seen at $Q \sim 1.75$ Å^{-1} and, just visible in the MAPS data, at $\sim$2.4 Å^{-1}. Neutron powder diffraction shows that these Q points correspond to magnetic Bragg peaks, with the strongest peak being the (010) at $Q \sim 0.6$ Å^{-1} [15].

The magnetic scattering appears to have an energy gap at this Q. The gap is most clearly seen in the MARI data with $E_i = 30$ meV. A subset of the corresponding data in Fig. 2 are shown on an expanded scale in Fig. 3. The size of the gap is difficult to estimate precisely from these data. However, measurements on BRISP and MARI with smaller E_i allow a lower limit to be placed. The energy and momentum transfers are coupled for neutrons. For a given incident neutron energy E_i and range of scattering angles ϕ, kinematic conditions limit the range of energy transfers that can be measured for a given Q. Measured data from BRISP, with $E_i = 20.45$ meV, and MARI, with $E_i = 15$ meV, are also shown in Fig. 3. The maximum achievable energy transfers at $Q = 0.6$ Å^{-1} are 7.3 and 5.8 meV for BRISP and MARI, respectively. Neither data set shows any clear magnetic signal, suggesting that the gap must be $\gtrsim$7 meV. The presence of a spin wave gap establishes that $NiPS_3$ has a finite magnetic anisotropy Δ. It was impossible to estimate the phonon contribution for the BRISP data due to the absence of a detector at high Q, hence none of the data in Fig. 3 have had a phonon estimation subtracted.

Figure 4 shows the MAPS data as a function of E, summed over various ranges of ϕ. The data have had the estimated phonon contribution subtracted and the contribution for each range, as determined by the method described in the appendix, is also shown in the figure. The phonon contribution becomes

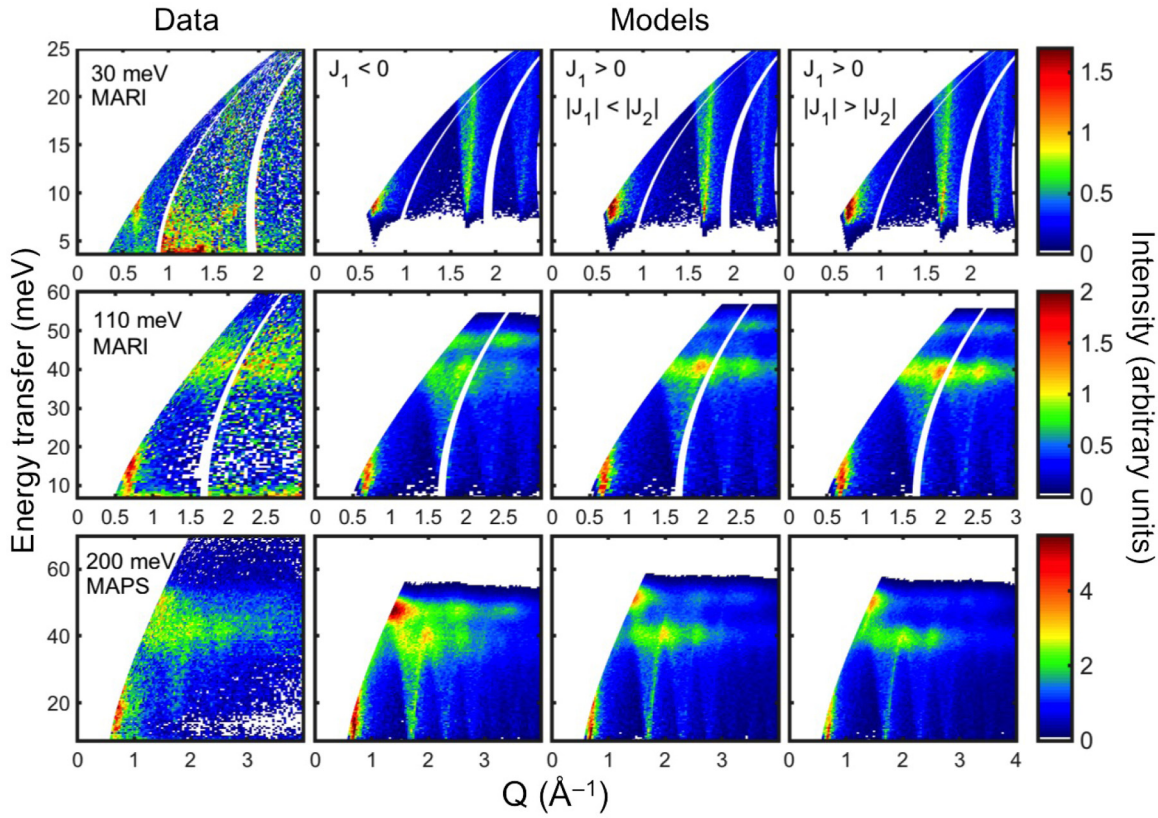

FIG. 2. Neutron inelastic data of $NiPS_3$ measured on the MARI and MAPS spectrometers for a selection of different incident energies, along with the calculation for models with different fitted parameters. The data were measured at a temperature of 5 K. Estimates for the phonon contributions, following the appendix, have been subtracted from the data.

large below ∼30 meV, with a peak at ∼15 meV. The estimated magnetic contributions show a dip at approximately the same energy, with the data for $15^\circ < \phi < 25^\circ$ even showing negative intensities. The phonon subtraction is notoriously difficult to get right at these energies, and the dip indicates that the phonon contribution is slightly overestimated in the $10 \leqslant E \leqslant 20$ meV energy range. The overestimation is more problematic at larger scattering angles where the phonon contribution is stronger and the magnetic contribution is weaker. For this reason, the fitting concentrated on the data for $\phi < 5^\circ$ where the influence of any phonon overestimation is minimized.

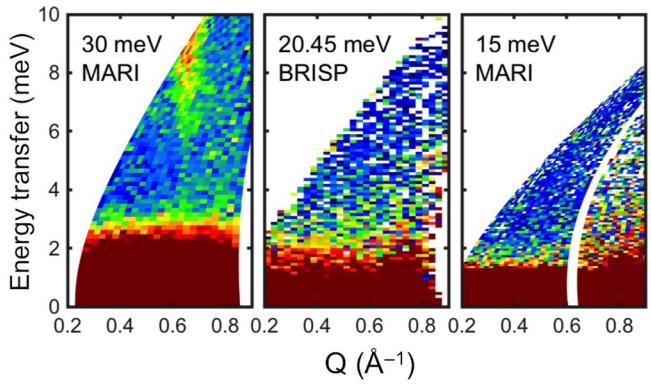

FIG. 3. Neutron inelastic data for $NiPS_3$ at low-energy transfers measured on the BRISP and MARI spectrometers for incident neutron energies of 20.45 and 15 meV, respectively. The sample temperatures were 1.5 K on BRISP and 5 K on MARI. Estimates for the phonon contributions have not been subtracted from the data.

The magnetic intensity shows substantial spectral weight from $35 \lesssim E \lesssim 55$ meV. The spectral weight appears to form two broad bands: one centered at $E \sim 40$ meV and the other at $E \sim 50$ meV. The bands are readily apparent in Fig. 4. The spectral weight in the $E \sim 50$ meV band is greater than for the $E \sim 40$ meV band at the smallest ϕ, however, the reverse is true for larger ϕ. This shift in the spectral weight between the two bands proved to be essential in determining the best estimate for the magnetic exchange interactions.

Exchange interactions up to the third nearest neighbor had to be included in the fits in order to have any reasonable comparison with the data. The necessity of including J_3 in the fits was not unexpected, as this was also required to fit the spin-wave dispersions of $MnPS_3$ [10] and $FePS_3$ [12,13]. The values for J_3 proved to be very robust on fitting, consistently giving values of ~ -6.5 meV irrespective of the chosen range of (ϕ, E). The fits establish J_3 to be large and antiferromagnetic and to be the dominant exchange in $NiPS_3$.

The fitted values for the anisotropy also proved to be robust, giving values of $\Delta \sim 0.3$ meV and establishing the single-ion anisotropy to have an easy axis. The sign of Δ was not constrained in the fits. Solutions with an easy axis anisotropy, given by $\Delta < 0$, were permitted, but were never found in the fit results. Subsequent calculations show that the

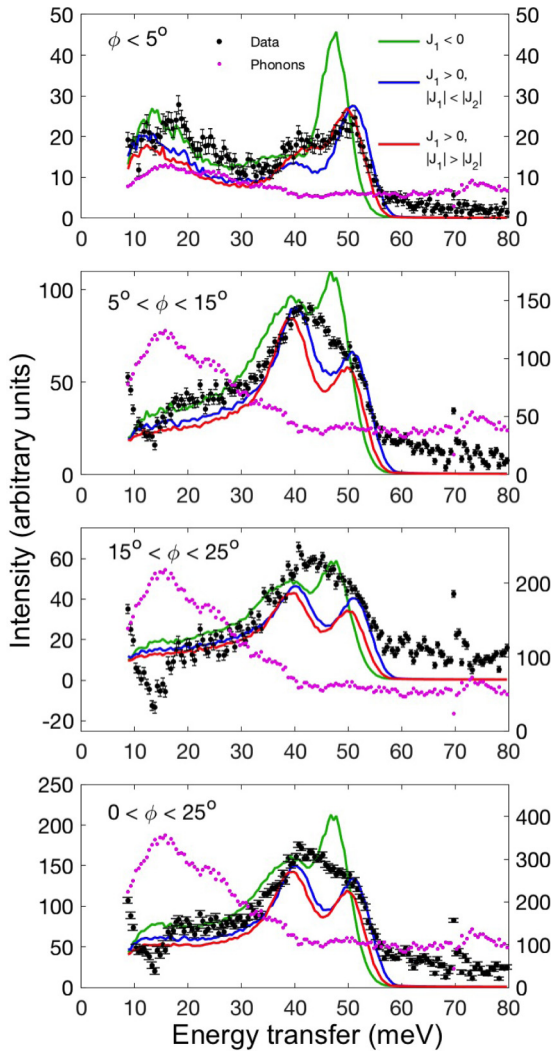

FIG. 4. Magnetic $I(E)$ data, measured using MAPS with $E_i = 200$ meV, integrated over different ranges of the scattering angle, ϕ. Models with the exchange parameters from various fits are also shown, along with the estimated phonon contribution that had been subtracted from the total scattering.

magnon energies become imaginary if Δ is constrained to be negative.

Previous analysis of the magnetic properties of $NiPS_3$ concluded that the anisotropy is easy-plane [17], based on the observation of anisotropy in the paramagnetic susceptibility. More recent measurements suggest that this is an artefact depending on how the sample was mounted in the magnetometer, and that the paramagnetic susceptibility is in fact isotropic [15]. Analysis of an isotropic susceptibility gives no preference for the sign of Δ, and can even be carried out in the pure Heisenberg limit with $\Delta = 0$ [9]. A proposed easy-axis anisotropy for $NiPS_3$ is not invalidated by its paramagnetic susceptibility.

An easy-axis anisotropy is, however, more consistent with the ordered magnetic structure. The ordered moments in $NiPS_3$ are not coplanar. They are collinear, pointing largely along the a axis with a small component normal to the ab planes [15]. The small component is enough to break the symmetry and make an easy-axis anisotropy the more logical conclusion for an analysis based on the Hamiltonian in Eq. (1).

TABLE I. Table showing the fit parameters used to calculate the expected neutron inelastic scattering in Figs. 2 and 4 and the magnon dispersions in Fig. 5. All values are in meV.

	$J_1 < 0$	$J_1 > 0$ $\lvert J_1\rvert < \lvert J_2\rvert$	$J_1 > 0$ $\lvert J_1\rvert > \lvert J_2\rvert$
J_1	−0.37	0.87	1.84
J_2	−1.98	−1.38	−0.18
J_3	−6.22	−6.55	−6.95
Δ	0.41	0.30	0.29
E_Γ	9.44	7.66	6.79
E_C	7.79	7.04	7.28

Determining values for J_1 and J_2 from the fits proved to be more ambiguous. Previous analysis of the magnetic susceptibility gave an exchange of −5.0 meV [17], i.e., an antiferromagnetic exchange, however, this estimate reflects the average exchange over all nearest neighbors. Stability phase diagrams have been generated for the magnetic structures on a honeycomb lattice with up to three nearest neighbors [28–30]. For appropriate ratios of J_2/J_1 and J_3/J_1, the magnetic structure for $NiPS_3$ is stable for either sign of J_1.

Fits were performed constraining $J_1 < 0$, $J_1 > 0$, and with no constraint on the sign of J_1. The MARI data could be fitted equally well with either a positive or negative J_1. The values for J_2 would change accordingly, with a relation that empirically appeared to be $J_1 - J_2 \approx 2$ meV.

The ambiguity was lifted on close inspection of fits to the MAPS data. MAPS has significantly better energy resolution that MARI, and measurements using a higher incident neutron energy gave access to high energies at smaller Q. Figure 4 shows the calculated magnetic inelastic scattering for the MAPS data using a selection of parameters resulting from separate fits to MARI and MAPS data. The parameters are given in Table I. All the fitted parameters in the table are consistent with the magnetic structure of $NiPS_3$, as given by the calculated stability phase diagrams [28–30].

All the fits give two peaks in the intensity from $35 \lesssim E \lesssim 55$ meV. The MARI data had insufficient resolution to differentiate the spectral weight in each of the peaks. However, they are more clearly seen in the MAPS data and it is clear that their spectral weights are best fitted by models with $J_1 > 0$, i.e., a ferromagnetic exchange. The conclusion becomes more apparent when comparing the data in Fig. 4 for $\phi < 5^\circ$, where the shift in spectral weight between the two peaks is reproduced for $J_1 > 0$ while only one clear peak is seen for fits with $J_1 < 0$. Due to kinematic constraints, the region of (Q, E) space where the shift in the spectral weight occurs was not accessible in the MARI data.

Figure 2 also shows the calculated scattering for the model parameters in Table I. A qualitative inspection shows that the models with $J_1 > 0$ better resemble the measured data.

Two fits with $J_1 > 0$ are shown in Fig. 4: one with $|J_1| < |J_2|$ and one with $|J_1| > |J_2|$. The fits are practically identical if they are compared for $\phi > 5^\circ$. This is also apparent when

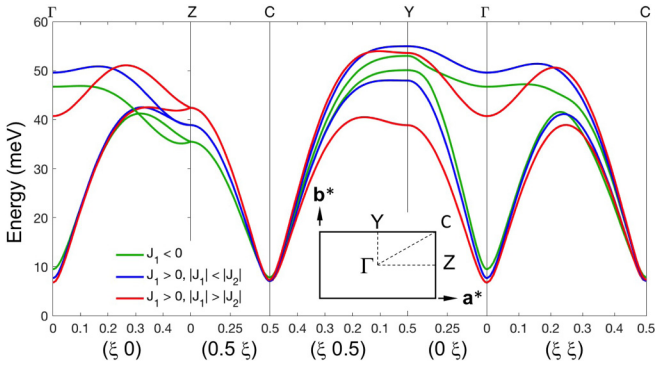

FIG. 5. The magnon dispersion along different trajectories in the Brillouin zone for the models listed in Table I. All the trajectories are given with respect to the crystallographic unit cell. The Brillouin zone and the relevant positions are shown in the insert.

comparing the calculated intensities in Fig. 2, with the two models being almost indistinguishable for the two sets of MARI data. However, the fits with $|J_1| > |J_2|$ compare better with the data for $\phi < 5^\circ$ and, indeed, the corresponding panel explicitly shows the results of the fit to these data. This (Q, E) region was only accessible with sufficient resolution using MAPS.

The preference is confirmed on comparing the calculated magnon energies for the different fit parameters. Figure 5 shows the magnon dispersions for different trajectories around the Brillouin zone, calculated using the parameters in Table I. The dispersions show a number of common features. All the dispersions have two doubly-degenerate magnon branches throughout the Brillouin zone, except at the Brillouin zone boundary between points Z and C where all the magnons are degenerate.

The magnon energies at C, in the Brillouin zone corner, are of particular note. All the calculations show a clear minimum at this point, which is similar in magnitude to the minimum at the Brillouin zone center. For the magnetic structure to be stable, however, the minimum energy in the magnon dispersion must be at the Brillouin zone center. This consideration allows extra constraints to be placed on the exchange parameters.

The magnon energies are given by the eigenvalues of Eq. (3), which take the form

$$\frac{E_{\mathbf{q}}^2}{4S^2} = A^2 + |B|^2 - C^2 - |D|^2 \pm (4|AB^* - CD^*|^2 - |BD^* - DB^*|)^{\frac{1}{2}}. \quad (4)$$

The energy of the lowest magnons at the Brillouin zone center is thus given by

$$E_\Gamma = 2S(\Delta(\Delta - 2J_1 - 8J_2 - 6J_3))^{\frac{1}{2}} \quad (5)$$

and the energy at C is given by

$$E_C = 2S(\Delta(\Delta + 2J_1 - 6J_3))^{\frac{1}{2}}. \quad (6)$$

Applying the condition $E_\Gamma < E_C$ leads to the inequality

$$J_1 > -2J_2. \quad (7)$$

The calculated values for E_Γ and E_C are shown in Table I. All the parameters give an energy gap comparable to the lower limit suggested by Fig. 3, i.e., $E_\Gamma \gtrsim 7$ meV. However, the inequality is respected only in the case of $J_1 > 0$, $|J_1| > |J_2|$. Thus J_1 is relatively large and positive and J_2 is relatively small and, most likely, negative.

TABLE II. Table showing the estimates for the anisotropies and exchange parameters, given in meV, for $MnPS_3$ [10], $FePS_3$ [13], and $NiPS_3$.

	$MnPS_3$	$FePS_3$	$NiPS_3$
S	5/2	2	1
T_N	78 K	120 K	155 K
J_1	−0.77(9)	1.46(1)	1.9(1)
J_2	−0.07(7)	−0.04(4)	−0.1(1)
J_3	−0.18(1)	−0.96(5)	−6.90(5)
J'	0.0019(2)	−0.0073(3)	–
Δ	0.0086(9)	2.66(8)	0.3(1)

Numerous fits were attempted with the added constraint of Eq. (7), including fixing $J_2 = 0$, over different ranges of (ϕ, E). Fixing $J_2 = 0$ gave a fit result that was almost indistinguishable from the result for $J_1 > 0$, $|J_1| > |J_2|$ shown in Fig. 4. While the errors on the parameters from an individual fit were typically in the second decimal place, the best estimate for the final values and their uncertainties comes from the spread in the fitted parameters over different fits. The final parameters may be taken to be $J_1 = 1.9 \pm 0.1$ meV, $J_2 = -0.1 \pm 0.1$ meV, $J_3 = -6.90 \pm 0.05$ meV, and $\Delta = 0.3 \pm 0.1$ meV, giving energies of $E_\Gamma = 6.81$ meV and $E_C = 7.39$ meV.

V. DISCUSSION

The best estimates for the magnetic exchange parameters and the anisotropy of $NiPS_3$ are listed in Table II. Noting that a honeycomb lattice has three first nearest neighbors, six second nearest neighbors, and three third nearest neighbors, the weighted sum of these parameters is −5.2 meV, which compares favorably with −5.0 meV, being the average value of the exchange determined from the analysis of the magnetic susceptibility [17]. A comparison with the calculated stability phase diagram [28–30] shows that the parameters are consistent with the magnetic structure of $NiPS_3$. The exchange parameters can also be used to estimate the Néel, T_N, and Curie-Weiss, Θ, temperatures for $NiPS_3$. Mean-field theory gives the following relations:

$$k_B\Theta = \tfrac{2}{3}S(S+1)(3J_1 + 6J_2 + 3J_3),$$
$$k_B T_N = \tfrac{2}{3}S(S+1)(J_1 - 2J_2 - 3J_3). \quad (8)$$

Substituting the values from Table II gives $\Theta = -241$ K and $T_N = 353$ K. The calculated Curie-Weiss temperature is remarkably close to previously published values of $\Theta = -241$ and $\Theta = -254$ K [9], providing confidence that the estimates for the exchange parameters are broadly correct. The calculated Néel temperature is more than twice the measured T_N, however, this is often the case for compounds that exhibit strong critical fluctuations where mean-field theory will break down. A similar difference was observed for $MnPS_3$ [10], where critical fluctuations are very strong [11]. The broad

maximum in the susceptibility for $NiPS_3$ [15] is also seen in $MnPS_3$ [9], hence critical fluctuations are also likely to be very strong in the nickel compound.

Ab initio calculations have been performed to estimate the electronic and magnetic properties of a broad range of transition metal-PS_3 compounds down to monolayer thickness, including $NiPS_3$ [31]. The calculation was performed using a Heisenberg Hamiltonian, similar to Eq. (1), without an anisotropy term. The calculated magnitudes for $NiPS_3$ differ quantitatively from the estimates presented here, however, they show qualitative agreement. The calculations show a ferromagnetic J_1, a J_2 with a substantially smaller magnitude, and a much larger, antiferromagnetic J_3. There is quantitative agreement between the ratios J_3/J_1, which are -3.2 to -4.2 for the calculations depending on the method, and are -3.6 for the values in Table II.

Table II also lists the magnetic exchange parameters and anisotropy for $MnPS_3$ and $FePS_3$. A comparison of the values for the three compounds shows an interesting evolution of the exchange parameters with the spin on the 2+ transition metal ion. The magnitudes of all the exchanges but J_2 increase with decreasing spin, which is also reflected in the magnitudes of the Néel temperatures. All the compounds are antiferromagnets, but only $MnPS_3$ has a nearest-neighbor exchange that is antiferromagnetic, i.e., negative. Such an exchange is consistent with the $\mathbf{k}_M = 0$ magnetic structure of $MnPS_3$, with each magnetic moment antiferromagnetically coupled with all three of its nearest neighbors. J_1 is positive, and therefore ferromagnetic, for $FePS_3$ and $NiPS_3$. Their magnetic structures are stabilized by the strong antiferromagnetic third nearest-neighbor exchanges. J_3 is particularly strong for $NiPS_3$ where it is the dominant exchange. The values for J_2 are close to zero for all the compounds.

The magnetic interactions in the compounds shown in Table II have been analyzed using the Goodenough-Kanamori rules [32] in an article by Le Flem *et al.* [33], published not long after the magnetic structures for these phases were determined and before any inelastic neutron scattering studies were performed. It is worth reviewing the discussion by Le Flem *et al.*, with some additional comments, with reference to the values now shown in Table II.

The magnetic interactions will be mediated by superexchange couplings, most likely through sulfur atoms, with additional direct exchange for interactions between nearest neighbors. Direct interactions will contribute to the sign and magnitude of J_1. Le Flem *et al.* demonstrate that the direct exchange will be antiferromagnetic in $MnPS_3$ and ferromagnetic for $FePS_3$ [33], in agreement with the sign of J_1 in Table II. Direct exchange does not exist for $NiPS_3$ as the relevant overlapping t_{2g} orbitals are filled for Ni^{2+} [33].

Superexchange couplings will also contribute to J_1, and superexchange pathways will mediate the interactions between further neighbors. Figure 6 shows part of the crystal structure for the transition metal-PS_3 compounds [3], showing those atoms closest to the *ab* planes. Selected transition metal atoms are marked with M while selected sulfur atoms are marked with S. Each M atoms has an approximately octahedral coordination with its neighboring S atoms.

The superexchange interaction between nearest neighbors will be mediated through the two S atoms on edge-shared

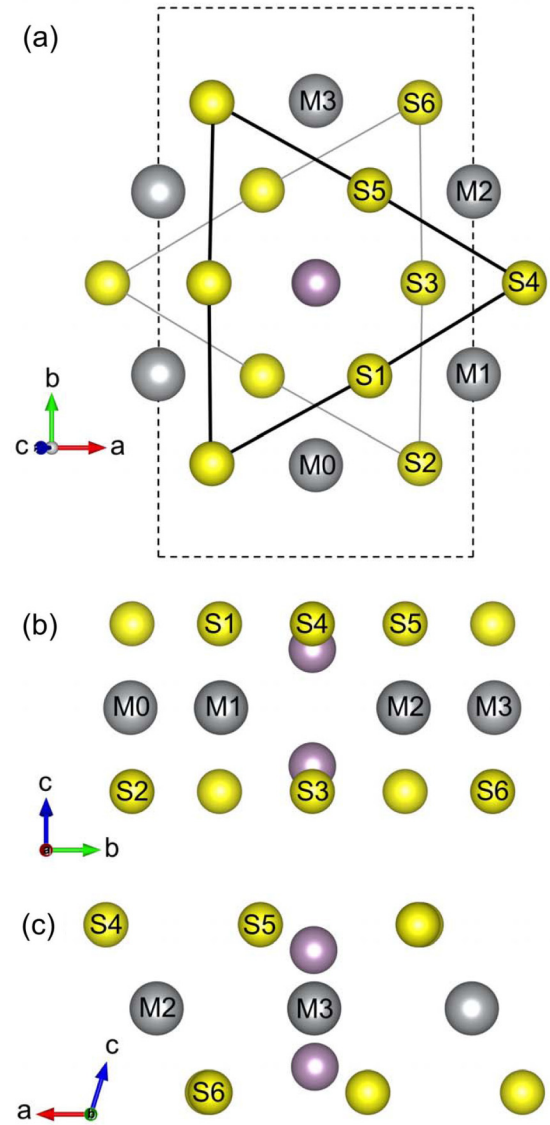

FIG. 6. Schematic showing the atoms close to the *ab* plane for transition metal-PS_3 compounds. The transition metal atoms are shown in grey, the sulfur atoms in yellow, and the phosphorus in purple. (a) shows the projection when viewing along $\mathbf{c}^\star$, with sulfur atoms above the *ab* plane connected with black lines and sulfur atoms below the plane connected with grey lines. The dashed line shows the size of the monoclinic unit cell in the *ab* plane. Selected metal atoms are marked as $M0, \ldots, M2$, and selected sulfur atoms are marked as $S1, \ldots, S6$. (b) and (c) show views along the **a** and **b** axes, respectively, with the same atoms marked. Note that some of the marked atoms will hide others when viewed along certain axes. The figure was created using the VESTA program [16].

octahedra between neighboring M atoms, for example, $S1$ and $S2$ between atoms $M0$ and $M1$ in Figs. 6(a) and 6(b). As discussed by Le Flem *et al.*, the nearest-neighbor interaction is purely due to superexchange in $NiPS_3$ [33]. The $M0$-S-$M1$ angle is $\sim 85^\circ$. The Goodenough-Kanamori rules suggest that the overall interaction for Ni^{2+}-Ni^{2+} and Fe^{2+}-Fe^{2+} should be ferromagnetic [32], as is observed. The same rules state that the Mn^{2+}-Mn^{2+} interaction tends towards antiferromag-

netism, which is consistent with the observations for $MnPS_3$ and the conclusions of Le Flem *et al.* [33].

There is no easy superexchange route for second nearest neighbors. As shown in Fig. 6, the path between $M0$ and $M2$ would need to pass through two S atoms. The path through $S1$ and $S3$ is highly unlikely because, as can be seen in Fig. 6(b), $S1$ is above the ab plane and $S3$ is below the plane. Paths along $S1$-$S4$ and $S1$-$S5$ are also unlikely. While these atoms are above the ab plane, the $M0$-$S1$-$S(4,5)$-$M2$ paths are not coplanar implying that nonoverlapping orbitals would need to be involved. The lack of a superexchange pathway would explain why J_2 is close to zero for all the compounds in Table II.

A superexchange pathway is available for third nearest neighbors. Figures 6(a) and 6(c) show that the $M0$-$S1$-$S5$-$M3$ path is coplanar and involves two atoms above the ab plane. As concluded by Le Flem *et al.*, these super-super-exchange pathways must be antiferromagnetic [33], and the values for J_3 in Table II confirm the conclusion. A detailed calculation of the exchange pathways will be the subject of future work.

A comparison of the anisotropies, Δ, is also interesting. $MnPS_3$ has a very small anisotropy, most likely dominated by dipole-dipole interactions [34]. The small anisotropy is consistent with $MnPS_3$ having Heisenberg-like magnetism [11]. The anisotropy is very large for $FePS_3$, which explains the Ising-like nature of its magnetism [9]. $NiPS_3$ has a relatively small anisotropy, although the spin wave gap is relatively large due to the strength of its exchange parameters.

As previously mentioned, the anisotropy in $NiPS_3$ has been the subject of debate. The discrepancy may have less to do with the magnitude of Δ and more to do with the presence of the deep minimum in the spin wave dispersion at the C point in Fig. 5. This deep minimum suggests that the magnetic structure of $NiPS_3$ is close to an instability. $NiPS_3$ has almost a hexagonal symmetry [3], and the (010) and $(\frac{1}{2}\,\frac{1}{2}\,\bar{\frac{1}{3}})$ reciprocal lattice points both have $Q \approx 0.6$ Å^{-1} and approximately map onto one another by rotating the reciprocal lattice by 60°. Doing so would give a different magnetic structure with a propagation vector close to $\mathbf{k}_M = (\frac{1}{2}\,\frac{1}{2}\,\frac{1}{3})$. The possible instability may be coupled with the strong phonons found in the same energy range E_Γ and E_C, as demonstrated in Fig. 4 and in the appendix, leading to magnetostriction that distorts the magnetization if the crystal is physically constrained by, for example, glue [15].

With this in mind, some caution must be applied to the values determined from the experiments on powdered samples reported here. The act of grinding the samples into powder may cause sufficient distortion to influence the magnetism. Future efforts will focus on verifying the exchange parameters by measuring neutron scattering from single crystals.

In light of the apparent evolution shown in Table II, it is interesting to determine the corresponding parameters for $CoPS_3$ whose Co^{2+} carry $S = 3/2$. $CoPS_3$ has an antiferromagnetic structure that is almost identical to $NiPS_3$ and a Néel temperature similar to that of $FePS_3$ [14]. The paramagnetic susceptibility for $CoPS_3$ is anisotropic in a manner similar to $FePS_3$ [9], although the anisotropy is clearly different as the collinear axes for the ordered moments are almost orthogonal between the two compounds. $NiPS_3$, however, has no apparent anisotropy in its paramagnetic susceptibility.

The differences between magnetic properties of the MPS_3 compounds are the result of removing electrons one at a time from a half-filled d shell. The ability to change these properties in a relatively controlled manner shows that this family of antiferromagnets will serve as excellent examples of model magnets with a honeycomb lattice, particularly once the exchange parameters and anisotropy in $CoPS_3$ are quantified.

VI. CONCLUSIONS

Neutron inelastic scattering has been used to determine the strengths of the magnetic exchange interactions and the anisotropy in $NiPS_3$. The data were fitted using a Heisenberg Hamiltonian with a single-ion anisotropy, and it was assumed that there was no magnetic exchange between the ab planes. The best results are shown in Table II, showing that the first nearest-neighbor exchange is ferromagnetic, the second-nearest neighbor exchange is small, and the third-nearest neighbor exchange is very large and antiferromagnetic. The measurements also establish the presence of a small easy-axis anisotropy, giving rise to an energy gap of ∼7 meV. The analysis shows that a similar gap should be found in the Brillouin zone corner, suggesting that $NiPS_3$ is close to a magnetic instability.

ACKNOWLEDGMENTS

The MAPS (Proposal No. RB1620017) and MARI (Proposal No. RB1510399) experiments at the ISIS Neutron and Muon Source were supported by a beamtime allocation from the Science and Technology Facilities Council (UK). The authors wish to thank the Institut Laue-Langevin for the use of their instruments. A.R.W. would like to thank B. Fåk for stimulating discussions. D.L. and A.R.W. thank H. Rønnow for financial support and for a critical reading of the manuscript.

APPENDIX: PHONON SUBTRACTION METHOD

The Q dependence of the neutron scattering cross-section can be used to estimate the phonon contribution from the measured scattering. The contribution can then be subtracted from the data and the remaining signal can be considered to be purely magnetic.

The cross-section for phonons increases as $\sim Q^2$ for small momentum transfers, eventually decreasing as $\sim \exp(-WQ^2)$ due to the Debye-Waller factor [35], The magnetic scattering, however, varies as the magnetic form factor squared which, for Ni^{2+}, decreases monotonically with increasing Q. The scattering may thus be considered to be purely due to phonons at sufficiently large Q.

Figure 7 shows the neutron scattering data from MAPS over the full measured Q range. The magnetic inelastic scattering is visible at small Q, and it soon becomes swamped by the phonon contribution. The phonon contribution was estimated in a two-step process.

The first step determined the Q dependence of the phonon contribution. Inspection of the data shows a reasonable density of phonon states from $70 \leqslant E \leqslant 120$ meV, which is greater than the maximum energy for the magnetic scattering. These data were extracted and the intensities for each energy

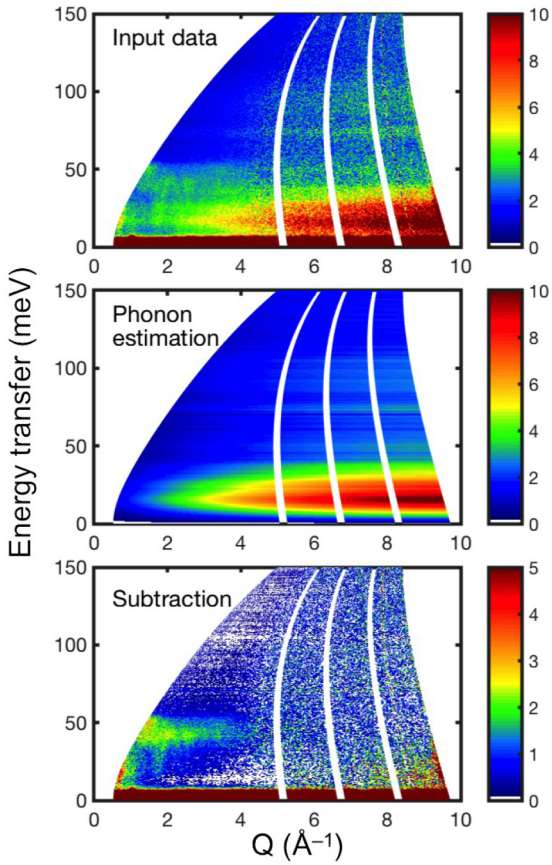

FIG. 7. Neutron inelastic scattering from $NiPS_3$ measured at 4 K on MAPS with $E_i = 200$ meV, the estimated phonon contribution to the data, and the MAPS data with the estimated contribution subtracted.

bin were fitted with the equation

$$I(Q, E) = Z_p(E)(p_1 + p_2 Q^{p_4} \exp(-p_3 Q^2)), \qquad \text{(A1)}$$

where $p_{1,\ldots,3}$ were global fit parameters and $Z_p(E)$ is an amplitude for the phonons with energy E. The exponent p_4 should nominally be equal to 2, however, setting $p_4 = 1$ resulted in better fits to the data and this value was chosen for the subsequent data treatment. The need to decrease p_4 may be understood as being the result of phonon multiple scattering in the sample. The global parameters were found to be $p_1 = 0.146$, $p_2 = 0.597$, and $p_3 = 0.0047$.

The phonons over the entire energy range were assumed to have the same Q dependence. The second step was therefore to determine the values of $Z_p(E)$ for all E. These were determined using the scattering at large Q. The range $7 \leqslant Q \leqslant 8$ Å^{-1} was chosen for the MAPS data. The detectors in this range were free from some spurious effects that were apparent at larger Q, and the Ni^{2+} magnetic form factor squared for $Q > 7$ Å^{-1} is less than 0.002 [36]. These data were extracted and fitted using Eq. (A1) with $Z_p(E)$ being the only free parameter.

The method to estimate the phonon contribution becomes unreliable at low energies due to contamination from the elastic scattering. Consequently, the method was only applied for energies above a minimum that was judged to be free from elastic contamination, which was chosen as 10 meV for the MAPS data. The phonon contribution was assumed to vary linearly with E below this energy, matching the gradient of the estimated phonon contribution for $10 \leqslant E \leqslant 13$ meV and becoming zero at the elastic line.

The estimated phonon contribution for the MAPS data is shown in Fig. 7 along with the result of its subtraction from the experimental data. There was some oversubtraction, particularly in the range of $E \sim 20$ meV, which represented the peak in the phonon density of states. The values of $Z_p(E)$ were therefore multiplied by 0.9 to reduce the oversubtraction.

The data in the subtraction plot shown in Fig. 7 were used in the fitting. A similar procedure was used for the MARI data. The phonon-subtracted data from both instruments are shown in Fig. 2.

[1] R. Brec, Solid State Ionics **22**, 3 (1986).
[2] V. Grasso and L. Silipigni, Riv. Nuovo Cimento **25**, 1 (2002).
[3] G. Ouvrard, R. Brec, and J. Rouxel, Mater. Res. Bull. **20**, 1181 (1985).
[4] C. R. S. Haines, M. J. Coak, G. I. Lampronti, C. Liu, H. Hamidov, A. R. Wildes, D. Daisenberger, P. Nahai-Williamson, and S. S. Saxena, arXiv:1801.10089.
[5] Y. Wang, J. Ying, Z. Zhou, J. Sun, T. Wen, Y. Zhou, N. Li, Q. Zhang, F. Han, Y. Xiao, P. Chow, W. Yang, V. V. Struzhkin, Y. Zhao, and H.-K. Mao, Nat. Commun. **9**, 1914 (2018).
[6] J. G. Park, J. Phys.: Condens. Matter **28**, 301001 (2016).
[7] M. A. Susner, M. Chyasnavichyus, M. A. McGuire, P. Ganesh, and P. Maksymovych, Adv. Mater. **29**, 1602852 (2017).
[8] F. Wang, T. A. Shifa, P. Yu, P. He, Y. Liu, F. Wang, Z. Wang, X. Zhan, X. Lou, F. Xia, and J. He, Adv. Funct. Mater. **28**, 1802151 (2018).
[9] P. A. Joy and S. Vasudevan, Phys. Rev. B **46**, 5425 (1992).
[10] A. R. Wildes, B. Roessli, B. Lebech, and K. W. Godfrey, J. Phys.: Condens. Matter **10**, 6417 (1998).
[11] A. R. Wildes, H. M. Rønnow, B. Roessli, M. J. Harris, and K. W. Godfrey, Phys. Rev. B **74**, 094422 (2006).
[12] A. R. Wildes, K. C. Rule, R. I. Bewley, M. Enderle, and T. J. Hicks, J. Phys.: Condens. Matter **24**, 416004 (2012).
[13] D. Lançon, H. C. Walker, E. Ressouche, B. Ouladdiaf, K. C. Rule, G. J. McIntyre, T. J. Hicks, H. M. Rønnow, and A. R. Wildes, Phys. Rev. B **94**, 214407 (2016).
[14] A. R. Wildes, V. Simonet, E. Ressouche, R. Ballou, and G. J. McIntyre, J. Phys.: Condens. Matter **29**, 455801 (2017).
[15] A. R. Wildes, V. Simonet, E. Ressouche, G. J. McIntyre, M. Avdeev, E. Suard, S. A. J. Kimber, D. Lançon, G. Pepe, B. Moubaraki, and T. J. Hicks, Phys. Rev. B **92**, 224408 (2015).
[16] K. Momma and F. Izumi, J. Appl. Crystallogr. **44**, 1272 (2011).
[17] N. Chandrasekharan and S. Vasudevan, J. Phys.: Condens. Matter **6**, 4569 (1994).
[18] L. J. de Jongh and A. R. Miedema, Adv. Phys. **50**, 947 (2001).
[19] A. D. Taylor, M. Arai, S. M. Bennington, Z. A. Bowden, R. Osborn, K. Andersen, W. G. Stirling, T. Nakane, K. Yamada, and D. Welz, KEK Report 90-25, **2**, 705 (1991).

[20] T. G. Perring, A. D. Taylor, R. Osborn, D. M. Paul, A. T. Boothroyd, and G. Aeppli, *Proceedings of the 12th Meeting of the International Collaboration on Advanced Neutron Sources (ICANS XII), Cosener's House, Abingdon, Oxfordshire, UK, 24-28 May, 1993* (RAL, Didcot, UK, 1994), pp. I–60.

[21] F. Formisano, A. D. Francesco, E. Guarini, A. Laloni, A. Orecchini, C. Petrillo, W. C. Pilgrim, D. Russo, and F. Sacchetti, J. Phys. Soc. Jpn. **82**, SA028 (2013).

[22] O. Arnold, J. C. Bilheux, J. M. Borreguero, A. Buts, S. I. Campbell, L. Chapon, M. Doucet, N. Draper, R. Ferraz Leal, M. A. Gigg, V. E. Lynch, A. Markvardsen, D. J. Mikkelson, R. L. Mikkelsone, R. Miller, K. Palmen, P. Parker, G. Passos, T. G. Perring, P. F. Peterson, S. Ren, M. A. Reuter, A. T. Savici, J. W. Taylor, R. J. Taylor, R. Tolchenov, W. Zhou, and J. Zikovsky, Nucl. Instrum. Methods Phys. Res., Sect. A **764**, 156 (2014).

[23] D. Richard, M. Ferrand, and G. J. Kearley, J. Neutron Res. **4**, 33 (1996).

[24] E. M. Wheeler, R. Coldea, E. Wawrzyńska, T. Sörgel, M. Jansen, M. M. Koza, J. Taylor, P. Adroguer, and N. Shannon, Phys. Rev. B **79**, 104421 (2009).

[25] "Pychop", http://docs.mantidproject.org/nightly/interfaces/PyChop.html, accessed: 2018-08-1.

[26] J. Kennedy and R. Eberhart, in *Proceedings of ICNN'95 - International Conference on Neural Networks*, Vol. 4 (IEEE, Piscataway, NJ, 1995), pp. 1942–1948.

[27] E. Farhi, http://ifit.mccode.org/Optimizers.html, accessed: 2018-09-18.

[28] E. Rastelli, A. Tassi, and L. Reatto, Physica B **97**, 1 (1979).

[29] E. Rastelli, A. Tassi, and L. Reatto, J. Magn. Magn. Mater. **15-18**, 357 (1980).

[30] J. B. Fouet, P. Sindzingre, and C. Lhuillier, Eur. Phys. J. B **20**, 241 (2001).

[31] B. L. Chittari, Y. Park, D. Lee, M. Han, A. H. MacDonald, E. Hwang, and J. Jung, Phys. Rev. B **94**, 184428 (2016).

[32] J. Kanamori, J. Phys. Chem. Solids **10**, 87 (1959).

[33] G. L. Flem, R. Brec, G. Ouvard, A. Louisy, and P. Segransan, J. Phys. Chem. Solids **43**, 455 (1982).

[34] C. Pich and F. Schwabl, J. Magn. Magn. Mater. **148**, 30 (1995).

[35] G. L. Squires, *Introduction to the Theory of Thermal Neutron Scattering* (Dover, Mineola, New York, 1996).

[36] P. J. Brown, in *International Tables for Crystallography*, edited by A. J. C. Wilson (Kluwer, Dordrecht, 1995), Vol. C, p. 391.